Magnetic structure of Fe-doped CoFe_{2}O_{4} probed by x-ray magnetic spectroscopies

J. A. Moyer, C. A. F. Vaz, D. A. Arena, D. Kumah, E. Negusse, and V. E. Henrich

Phys. Rev. B **84**, 054447 — Published 15 August 2011

DOI: 10.1103/PhysRevB.84.054447

Magnetic structure of Fe-doped $CoFe_2O_4$ probed by x-ray magnetic spectroscopies

J. A. Moyer[1], C. A. F. Vaz[1,*], D. A. Arena[2], D. Kumah[1], E. Negusse[3] and V. E. Henrich[1]

[1]*Department of Applied Physics and Center for Research on Interface Structures and Phenomena, Yale University, New Haven, Connecticut 06511*
[2]*National Synchrotron Light Source, Brookhaven National Laboratory, Upton, New York 11973*
[3]*Department of Physics, Montana State University, Bozeman, Montana 59717*

The magnetic properties of iron-doped cobalt ferrite ($Co_{1-x}Fe_{2+x}O_4$) (001) thin films grown epitaxially on MgO (001) substrates are investigated by superconducting quantum interference device (SQUID) magnetometry and soft x-ray magnetic linear (XMLD) and circular (XMCD) dichroisms. All $Co_{1-x}Fe_{2+x}O_4$ ($0.01 \leq x \leq 0.63$) samples have out-of-plane magnetic easy axes and large coercive fields, unlike Fe_3O_4, due to a large Co^{2+} orbital moment. The magnetic moments for those samples are significantly reduced from their bulk values; however, as x increases, the magnetic moments tend nearer to their bulk values and increase more rapidly as x approaches 1. This reduction in magnetic moment is attributed to spin canting among the Co^{2+} cations, owing to a small in-plane tensile strain in the film, and to an increased antiferromagnetic alignment among all the cations caused by a partially inverse spinel cubic structure and the likely presence of anti-phase boundaries. Our results show that small changes in stoichiometry can lead to significant changes in the magnetic moment of $Co_{1-x}Fe_{2+x}O_4$, especially at large values of x.

I. INTRODUCTION

The search for new, functional spintronic materials and the goal of designing devices that utilize both the charge and spin of the electron to realize novel functionalities is the driving force behind much current research.[1, 2] One class of materials that is promising for use in spintronic devices is the 3*d* transition-metal complex oxides, which, owing to their highly correlated *d*

electrons, exhibit a wide variety of electronic and magnetic properties.[3, 4] These properties can often be tuned through small changes in strain or doping, such as the ferroelectric phase transition of $SrTiO_3$ upon application of strain[5] and the antiferromagnetic/ferromagnetic[6] and metal/insulator[7] phase transitions of $La_{1-x}Sr_xMnO_3$ (LSMO) upon change in doping. Examples of novel behavior in complex oxides include room temperature tunneling magnetoresistance of LSMO/$SrTiO_3$/LSMO[8] and Fe_3O_4/$CoCr_2O_4$/LSMO[9] magnetic tunnel junctions, the spin filter effect of $CoFe_2O_4$[10] and $NiFe_2O_4$[11], and electric field control of ferromagnetism through strain-driven magnetoelectric coupling of $CoFe_2O_4$/$BaTiO_3$ nanostructures[12] and LSMO/$BaTiO_3$ multilayers[13] and charge-driven magnetoelectric coupling in $PbZr_xTi_{1-x}O_3$/LSMO heterostructures.[14, 15]

One class of these complex oxides that has received much interest is the 3*d* transition-metal spinel ferrites, MFe_2O_4 (M = 3*d* transitional metal cation). These materials have the spinel crystal structure [see Fig. 1(a)] in which 1/3 of the cations are tetrahedrally coordinated and 2/3 of the cations are octahedrally coordinated. The crystal structure is normal spinel if all the 2+ cations are located in tetrahedral sites and inverse spinel if the 2+ cations occupy octahedral sites. The spinel ferrites are environmentally stable, with widely varying magnetic properties, magnetic critical temperatures (T_c) much higher than room temperature, and large predicted spin polarizations.[16-21] Of the stoichiometric spinel ferrites, only magnetite (M = Fe, Fe_3O_4) is electrically conducting, with a conductivity up to ten orders of magnitude larger than the other 3*d* spinel ferrites (M = Mn, Co, Ni, Zn).[16, 22] However, upon Fe doping ($M_{1-x}Fe_{2+x}O_4$), the insulating ferrites become electrically conducting.[23-28] Although the resistivity and density of states near the Fermi energy of $M_{1-x}Fe_{2+x}O_4$ thin films behave systematically upon Fe doping, recent studies on the magnetic structure of $Zn_{1-x}Fe_{2+x}O_4$ have shown that the magnetic moment behaves non-

linearly with Fe doping and does not obey Néel's theory of ferrimagnetism.[26-28] This has been attributed to changes in the strength of the magnetic interactions among the different cations. This non-linear behavior has also recently been seen in the magnetic moment of $Co_{1-x}Fe_{2+x}O_4$ as measured by SQUID magnetometry.[24]

In this study, we report a detailed investigation into the nature of the magnetic structure of $Co_{1-x}Fe_{2+x}O_4$ over a doping range of $0.01 \leq x \leq 1$. SQUID magnetometry is used to determine the magnetic easy axes, while site-specific XMLD and XMCD allow for investigations into the magnetic properties of the individual cations. We find that the magnetic properties of $Co_{1-x}Fe_{2+x}O_4$ change markedly as x is increased from 0.01 to 1, as manifest most strikingly in a magnetic moment that is drastically reduced for $CoFe_2O_4$ and which increases non-linearly up to a nearly bulk value magnetic moment for Fe_3O_4. Three factors are responsible for these unique magnetic properties: strain; a partially inverse spinel crystal structure; and the likely presence of anti-phase boundaries. Our results and analysis show that a highly Fe-doped $Co_{1-x}Fe_{2+x}O_4$ thin film has unique magnetic properties that should make it an exciting candidate material for use in future spintronic devices.

To understand the magnetic structure of $Co_{1-x}Fe_{2+x}O_4$, it is helpful to begin with the magnetic structure of Fe_3O_4. Fe_3O_4 has a completely inverse spinel crystal structure, with the Fe^{3+} cations on the octahedral and tetrahedral sites coupled antiferromagnetically *via* the magnetic superexchange interaction, and the Fe^{2+} and Fe^{3+} cations on the octahedral sites coupled ferromagnetically through the magnetic double exchange interaction [Fig. 1(b)].[29] This ferrimagnetic alignment results in a measured bulk magnetic moment of 4.1 μ_B/formula unit (f.u.),[16] while theoretical calculations predict a magnetic moment varying between 3.65 and 4.43

μ_B/f.u., depending on the theoretical model.[17-21, 30] The coexistence of these two magnetic interactions gives Fe_3O_4 a high T_c of 858 K.[16]

$CoFe_2O_4$ is similar to magnetite, except that the Fe^{2+} cations are replaced by Co^{2+} cations. The crystal structure is no longer fully inverse like magnetite; while the majority of Co^{2+} cations occupy octahedral sites, a small fraction (2 – 24%, depending strongly on the thermal history of the sample)[31] are located on the tetrahedral sites.[24, 31, 32] The Fe^{3+} cations on the octahedral and tetrahedral sublattices are still antiferromagnetically coupled, while the Fe^{3+} and Co^{2+} cations are ferromagnetically coupled, resulting in a ferrimagnet [Fig. 1(c)]. In a perfectly inverse crystal, $CoFe_2O_4$ has been predicted by different theoretical models to have a spin magnetic moment between 2.73 and 3 μ_B/f.u,[17, 18, 21] whereas bulk $CoFe_2O_4$ has an experimentally determined magnetic moment of 3.7 μ_B/f.u.[16] T_c of the bulk has been measured to be 793 K.[16] However, thin films grown on higher symmetry substrates, such as MgO and $SrTiO_3$, show a reduced saturation magnetization of 25 – 60% of bulk values.[24, 33-36] $CoFe_2O_4$ is unique among the ferrites in that it has a large magnetic anisotropy owing to a spin-orbit stabilized ground state (with unquenched orbital momentum $l_z = \pm 1$) caused by a trigonal crystal field on the Co^{2+} octahedral cations.[33, 37-42] This results in a cubic magnetocrystalline anisotropy constant, K_1, that has a different sign and is over an order of magnitude larger than that of the other 3*d* transition-metal spinel ferrites, and a magnetostriction constant, λ_s, of opposite sign and nearly three times as large as that of Fe_3O_4.[16] Owing to this large magnetostriction, $CoFe_2O_4$ has been used extensively in strain-driven multiferroic ferroelectric-$CoFe_2O_4$ nanostructures, where a change in the polarization of the ferroelectric induces a lattice distortion on the $CoFe_2O_4$, resulting in a magnetization change. This has been realized with both $CoFe_2O_4$ nanopillars grown within a ferroelectric matrix[12, 43] and $CoFe_2O_4$ thin films grown epitaxially on ferroelectrics.[44, 45]

When $CoFe_2O_4$ is doped with extra iron to form $Co_{1-x}Fe_{2+x}O_4$, Fe^{2+} cations substitute solely for the Co^{2+} cations on the octahedral site, which results in a crystal structure that is more nearly inverse than $CoFe_2O_4$. Even though it has been shown that the resistivity and density of states near the Fermi energy vary smoothly with doping, the magnetic properties do not change in a predictable manner.[24] In particular, measurements on $Co_{0.1}Fe_{2.9}O_4$ particles show only small changes in K_1 from $CoFe_2O_4$ values, but large changes in λ_s.[46] Determination of the magnetic structure of $Co_{1-x}Fe_{2+x}O_4$ could lead to exciting possibilities for the field of spintronics and should help ascertain the cause for the reduced magnetic moment of thin-film $CoFe_2O_4$.

II. EXPERIMENTAL DETAILS

$Co_{1-x}Fe_{2+x}O_4$ (001) thin films (x = 0.01, 0.18, 0.39, 0.63, 1) were grown epitaxially on MgO (001) substrates using molecular beam epitaxy (MBE), with film thicknesses of ~ 20 nm. All samples were capped with 1 nm MgO to prevent surface oxidation after removal from UHV. A previous analysis of the structural properties, along with details on the thin film growth, determination of stoichiometry, and electronic structure, has been published elsewhere.[24] X-ray diffraction measurements (Cu $K\alpha$ line), using a Shimadzu diffractometer set in the parallel beam geometry, of 20 nm and 200 nm $Co_{1-x}Fe_{2+x}O_4$ (001) thin films had previously determined that all stoichiometries ($0 \leq x \leq 1$) are likely to have a small in-plane tensile strain due to a lattice mismatch of -0.3% between MgO and $Co_{1-x}Fe_{2+x}O_4$. Bulk magnetic properties were measured using a SQUID magnetometer (Quantum Design MPMS), while cation specific magnetic properties were investigated using soft x-ray magnetic linear dichroism (XMLD) and circular dichroism (XMCD). XMLD and XMCD measurements were performed on beamline U4B at the National Synchrotron Light Source (NSLS) at Brookhaven National Laboratory (spectra

measured in total electron yield mode) with energy resolutions of ~ 0.3 (0.4) eV for the XMLD (XMCD) measurements, respectively. The XMLD measurements were conducted with the samples at remnant magnetization and rotated with respect to the x-ray beam; x-ray absorption (XAS) measurements were taken at angles of 30^o, 45^o, 60^o, 75^o and 90^o between the **E**-field of the x-rays and the [001] crystal direction. The degree of circular polarization for the XMCD measurements was 70%, with the incident photons aligned parallel to the magnetic field and the [001] crystal direction, hence measuring the out-of-plane magnetic moments. The XMCD spectra were obtained by using a fixed helicity of light and reversing the applied magnetic field by pulsing it to 9.5 kOe and holding it at 3.5 kOe during the measurement. The XMCD measurements were conducted at 300 K, while the SQUID and XMLD measurements were conducted at both 100 and 300 K.

III. RESULTS

A. Bulk Magnetic Properties

The bulk magnetic properties were determined by measuring the magnetic response of each sample using a SQUID magnetometer. Figure 2 shows the in-plane and out-of-plane *M-H* loops measured at both 100 and 300 K for five samples with $0.01 \leq x \leq 1$. A diamagnetic substrate contribution, similar for all samples, was removed from the data. It is clear from the *M-H* loops that the magnetic properties of the $Co_{1-x}Fe_{2+x}O_4$ ($0.01 \leq x \leq 0.63$) samples are drastically different than the Fe_3O_4 ($x = 1$) sample, with the $Co_{1-x}Fe_{2+x}O_4$ ($0.01 \leq x \leq 0.63$) samples having notably larger coercive fields and smaller saturation magnetizations than the Fe_3O_4 sample. The magnetic easy axes are determined by comparing the in-plane and out-of-plane coercive fields [Figs. 3(a) and (b)]. The coercive fields of the $Co_{1-x}Fe_{2+x}O_4$ ($0.01 \leq x \leq$

0.63) samples are larger for the out-of-plane direction, while the coercive field of the Fe_3O_4 sample is larger in the in-plane direction, leading to the conclusion that the magnetic easy axes for the $Co_{1-x}Fe_{2+x}O_4$ ($0.01 \leq x \leq 0.63$) samples are out-of-plane, while the magnetic easy axis of the Fe_3O_4 sample is in-plane. This determination of the magnetic easy axes is in agreement with magnetoelastic anisotropy energy calculations for films under a slight in-plane tensile strain.[47, 48]

The in-plane and out-of-plane saturation and remnant magnetizations for all samples are compared at 100 K [Fig. 3(c)] and 300 K [Fig. 3(d)]. At both 100 and 300 K, the in-plane saturation magnetization of Fe_3O_4 is larger than the out-of-plane magnetization, with an in-plane value at 100 K of 495 emu/cm^3, which is slightly lower than the bulk value of 514 emu/cm^3.[16] This slight reduction in magnetic moment has been attributed to the presence of anti-phase boundaries in Fe_3O_4 thin films grown on higher symmetry substrates.[49] For the $Co_{1-x}Fe_{2+x}O_4$ ($0.01 \leq x \leq 0.63$) samples, there is no discernable difference between the in-plane and out-of-plane magnetizations at both 100 and 300 K, with the out-of-plane saturation magnetizations at 100 K increasing from 154 to 228 emu/cm^3 as x increases from 0.01 to 0.63. These values are significantly less than the bulk values, which, assuming a ferrimagnetic alignment between the octahedral and tetrahedral sites for all values of x, should increase linearly from 464 to 514 emu/cm^3 as x increases from 0 to 1.[16] However, the saturation magnetizations tend closer to the bulk values with increased x. This reduced magnetization has been extensively reported for $CoFe_2O_4$[33-36] and $Co_{1-x}Fe_{2+x}O_4$ ($x < 1$)[24] films grown on higher symmetry substrates.

B. X-ray Magnetic Linear Dichroism

Information on the direction of the spin axes for the individual cations has been obtained using XMLD, which is dependent on $\langle M^2 \rangle$ of the cations.[50] XAS measurements were taken

with the samples in an out-of-plane remnant magnetization state and for different angles between the **E**-field of the x-rays and the [001] crystal direction (30^o, 45^o, 60^o, 75^o and 90^o). All measurements were normalized to the Fe doping level of the sample, so that spectra of the same samples measured with different orientations between the **E**-field of the x-rays and the [001] crystal direction have the same integrated intensities. This allowed for a qualitative analysis of the relative changes between the different XMLD spectra, while eliminating any reduction in signal due to the angle of the incident x-rays relative to the surface normal (*i.e.* saturation effects). The spectra with the x-ray **E**-field perpendicular and parallel to the [001] crystal direction were determined by fitting the five measured spectra with the angle-dependent XAS equation:[29]

$$I(\theta) = I_{\parallel} \cos^2 \theta + I_{\perp} \sin^2 \theta \qquad (1)$$

from which $I_{\parallel}$ and $I_{\perp}$ spectra are interpolated.

Figure 4(a) shows the interpolated Co $L_{2,3}$ XAS spectra for the **E**-field perpendicular and parallel to the [001] crystal direction, along with the difference spectrum for the $Co_{0.37}Fe_{2.63}O_4$ sample, while Fig. 4(b) compares the XMLD spectra for the four samples with $x < 1$, taken at 300 K. The L_3 edge is characterized by a large negative peak at 776.3 eV, two positive peaks at 777.2 and 778.3 eV and a negative high energy shoulder, while the L_2 edge has a large positive peak at 792.9 eV and a small negative peak at 794.4 eV. The peaks of the $Co_{1-x}Fe_{2+x}O_4$ ($0.01 \leq x \leq 0.39$) samples all have similar intensities except for the low energy L_3 positive peak and L_2 positive peak of the $Co_{0.99}Fe_{2.01}O_4$ sample, which are larger. All peaks of the $Co_{0.37}Fe_{2.63}O_4$ sample have larger intensity compared with the other samples; the physical origin of this increased intensity will be discussed later. The extrapolated Fe $L_{2,3}$ XAS spectra and the XMLD spectrum for the $Co_{0.37}Fe_{2.63}O_4$ sample are shown in Fig. 5(a), with a comparison of the XMLD spectra of the samples with $x < 1$ shown in Fig. 5(b), taken at 300 K. Regions of interest are, in

the L_3 region, four negative peaks at 706, 707.5, 708 and 710.2 eV and two positive peaks at 707.7 and 708.8 eV, and, in the L_2 region, two negative peaks 718.7 and 720.5 eV and the two positive peaks at 719.8 and 722.3 eV. As x increases from 0.01 to 0.63, the four negative L_3 peaks all vary in amplitude, while the two positive peaks remain constant; in the L_2 region, the two low energy peaks increase in size, while the two high energy peaks remain constant. The changes in peak size increase markedly for the $x = 0.63$ sample. Measurements at 100 K yielded XMLD spectra almost identical to those in Figs. 4 and 5.

The dichroic effects in XMLD arise from charge anisotropies, which are caused by either a crystal field symmetry lower than cubic or the presence of a magnetic spin axis. Because of the high T_c of $Co_{1-x}Fe_{2+x}O_4$, it is not possible to separate these two effects by measuring the XMLD above T_c; instead, XMLD spectra were calculated using the Ligand Field Multiplet (LFM) model and compared with the experimental spectra.[51-53] The LFM model calculates the spectra for a cation in a given ligand field and a magnetic exchange field oriented along the c-axis. By calculating the spectra of the relevant cationic states, the total LFM spectrum for the $Co_{1-x}Fe_{2+x}O_4$ sample is obtained from a weighted superposition of the individual spectra of each cation; this can then be compared with the measured XMLD spectrum to determine which cation is responsible for which peak in the experimental spectrum. LFM calculations were performed using the CTM4XAS 5.0 program[54] including spin-orbit coupling, crystal field effects, and reduction of the Slater integrals $F(dd)$, $F(pd)$, and $G(pd)$ to include the interatomic configuration interaction.[55] The following parameters were obtained by comparing the LFM calculated spectrum with the experimental spectrum. The $2p$ and $3d$ spin-orbit interactions were reduced by multiplying by a factor of 0.98 and 0.75, respectively, for the cobalt cations, while full spin-orbit interactions were used for the iron cations. The $F(dd)$, $F(pd)$ and $G(pd)$ integrals were taken to

be 70%, 80% and 75% of the Hartree-Fock values, respectively, for the cobalt cations and 70%, 80%, and 80% respectively, for the iron cations. Octahedral crystals fields of 1.2 eV and 1.6 eV were used for the cobalt and iron cations, respectively, while tetrahedral crystals fields of 0.6 eV were used for both cobalt and iron cations. All Slater integral reductions and crystal field values are consistent with previous results on Fe_2O_3, Fe_3O_4, and $CoFe_2O_4$.[56-59] The cation site occupancies were taken from analysis of the XAS spectra.[24] All spectra were broadened by a Lorentzian with a half-width of 0.1 (0.3) eV for the L_3 (L_2) edge to account for core-hole lifetime broadening and by a Gaussian with a half-width of 0.34 eV to account for instrumental broadening.

Figures 4(c) and 5(c) show the LFM calculation for the $Co_{0.61}Fe_{2.39}O_4$ sample with cubic symmetry and an additional magnetic exchange field oriented along the [001] crystal direction. The experimental and LFM calculated spectra match quite well. Attempts to calculate spectra using a tetragonal distortion due to a tensile strain could not reproduce the experimental spectra. This modeling of the spectra thus allowed us to determine that the majority of the dichroic effects seen in the XMLD spectra result from the magnetic spin axes and not from the small tensile strain; therefore, all interpretations of the XMLD spectra will neglect any effects due to non-cubic crystal symmetries.

Since prior analysis of the XAS spectra of these samples concluded that there are only minor variations in the Co^{2+} tetrahedral/octahedral ratio with doping,[24] we conclude that the increase in peak intensity for the $Co_{0.61}Fe_{2.39}O_4$ sample is not caused by changes in the site occupancies, but by an increased alignment of the magnetic spin axes with the c-axis for the Co^{2+} cations. For the Fe cations, we know that increased doping causes an increase in number of Fe^{2+} octahedral cations. Examination of the individual iron cation LFM spectra in Fig. 5(c) shows

that the peaks in Fig. 5(b) that do not change in intensity with increased x are caused solely by the Fe^{3+} cations, whereas the change in intensity in the other peaks is due to an increase in the number of Fe^{2+} octahedral cations. However, it has been noted that the intensity of these peaks does not change linearly with increasing x. Hence, we conclude from the XMLD data that the alignment of the spin axes for the Fe^{3+} cations does not change, whereas there is an enhanced alignment of the spin axes of the Fe^{2+} cations with the [001] crystal direction with increasing x.

C. X-ray Magnetic Circular Dichroism

XMCD measurements were carried out to obtain information on the magnetic properties of the individual cations in our samples. Figure 6(a) shows the Co 2p XAS spectra with the magnetic field aligned in opposite directions and the corresponding XMCD spectrum for the $Co_{0.99}Fe_{2.01}O_4$ sample. All XMCD spectra are corrected to account for the degree of polarization of the x-rays, the Fe doping level, and the non-saturated magnetic moments through comparison with SQUID measurements, resulting in spectra that correspond to fully magnetized samples. Comparison of the Co XMCD $L_{2,3}$ spectra for the four different $Co_{1-x}Fe_{2+x}O_4$ samples with $x < 1$ are displayed in Fig. 6(b). The L_3 edge is characterized by a main peak at 778 eV and a small low energy peak at 776 eV, while the L_2 edge contains only one very broad peak spanning 792 – 796 eV. There is very little change in the spectra as x increases from 0.01 to 0.39, with only a slight increase occurring at the main L_3 peak; however, there is a large increase in dichroism for all three peaks for the $Co_{0.37}Fe_{2.63}O_4$ sample.

The Fe 2p XAS and XMCD spectra for the Fe_3O_4 sample are shown in Fig. 7(a); the Fe XMCD spectra were corrected in the same manner as the Co XMCD spectra. Figure 7(b) displays the corresponding Fe XMCD $L_{2,3}$ spectra along with the Fe_3O_4 spectra. The Fe XMCD

spectra contain much more structure than the Co spectra, with the L_3 region being the main region of interest; here there is a low energy shoulder around 705 eV, a low energy negative peak at 707 eV, a positive peak at 708 eV, a high energy negative peak at 708.9 eV, and a high energy shoulder spanning 710 – 714.5 eV. The L_2 region for the Fe_3O_4 sample also contains a great deal of structure, but the peaks are much smaller for the samples with $x < 1$ and the structure is mostly indistinguishable for these samples; thus, only the L_3 region will be used for analysis. Like the Co XMCD spectra, there is little change in the Fe L_3 XMCD spectra as x increases from 0.01 to 0.39, with the intensity of the low energy negative peak increasing slightly, while the intensities of the positive and high energy negative peaks both decrease. Then for the $x = 0.63$ and $x = 1$ samples, all peaks, except for the positive L_3 peak, show a substantial increase.

LFM calculations were performed for the XMCD spectra and compared with the experimental data. The same parameters were used for the XMCD spectra as in the XMLD spectra, except that the magnetic exchange fields for each cation were adjusted to match the main L_3 peak intensities of the experimental spectra and the instrumental broadening was accounted for by a Gaussian with a half-width of 0.45 (0.40) eV for the Co (Fe) spectra. Figure 6(c) shows the $Co_{0.99}Fe_{2.01}O_4$ experimental spectrum along with the individual Co^{2+} octahedral and tetrahedral LFM spectra and the $Co_{0.99}Fe_{2.01}O_4$ LFM spectrum. The Co^{2+} octahedral cation LFM spectrum has two peaks in the L_3 and a single, broad peak in the L_2 region, which correspond well with the experimental spectrum, as well as a high energy L_3 shoulder that is absent from the experimental spectrum. The tetrahedral cation has only one peak in both the L_3 and L_2 regions which reduces the intensity of the main L_3 and the L_2 peak. Table 1 contains the exchange field energies used for the calculations; owing to the small peak intensity arising from the Co^{2+} tetrahedral cations, large changes in the exchange field energies produced only small changes in

the spectrum, and we thus set the exchange field energies equal for both Co^{2+} cations. The exchange field energies used in the modeling represent the average exchange field energy per cation oriented along the [001] direction. These energies show that there is a small, approximately linear increase in the average exchange field with increasing doping for the $Co_{1-x}Fe_{2+x}O_4$ ($0.01 \leq x \leq 0.39$) samples and a large increase in average exchange field for the $Co_{0.37}Fe_{2.63}O_4$ sample. This is in agreement with the XMLD data, since an enhanced alignment of the spin axes with the [001] direction, as determined for the $Co_{0.37}Fe_{2.63}O_4$ sample from the XMLD analysis, will result in a greater alignment of the exchange field axis with the [001] direction, resulting in the need for a larger average exchange field energy in the LFM calculation.

The results of the LFM calculations for the Fe^{2+} octahedral, Fe^{3+} octahedral, and Fe^{3+} tetrahedral cations, along with the Fe_3O_4 experimental and LFM spectra, are shown in Fig. 7(c). The L_3 region is characterized by three sharp peaks and low and high energy shoulders; comparison with the LFM calculations allows us to determine which cations contribute to which peak. The Fe^{2+} octahedral cations are responsible for the low energy shoulder, a majority of the negative low energy peak, and a small fraction of the negative high energy peak; the Fe^{3+} octahedral cations are responsible for the a small part of the negative low energy peak and the majority of the negative high energy peak; and the Fe^{3+} tetrahedral cations are responsible for the positive central peak. All three cations contribute intensity to the high energy shoulder. The increase in Fe^{2+} cations can be seen clearly in the increase in the low energy shoulder and an increase in the ratio between the intensities of the two negative peaks. The exchange field energies used for the calculations are listed in Table 1. The behavior of the average exchange fields for the Fe cations is similar to that of the Co cations. The average exchange fields remain roughly constant for the $Co_{1-x}Fe_{2+x}O_4$ ($0.01 \leq x \leq 0.39$) samples, with a slightly decreasing trend,

but increasing by large amounts for the $Co_{0.37}Fe_{2.63}O_4$ and Fe_3O_4 samples. It is important to note that the exchange field energy of each cation used in the LFM model is an average of all the exchange field energies of that cation throughout the sample. When two cations of the same type (*i.e.* Fe^{3+} tetrahedral cations) are antiferromagnetically aligned, the average exchange field of these two cations will be zero since their exchange field energies will be of opposite sign. Hence, even a small fraction of antiferromagnetically aligned cations of the same type will result in a significantly reduced average exchange field energy. This reasoning can be used to explain that the very large increase in the average exchange field energies for the Fe_3O_4 sample is likely caused by an enhanced ferromagnetic alignment of the Fe cations within both the octahedral and tetrahedral sublattices compared with the $Co_{1-x}Fe_{2+x}O_4$ ($0.01 \leq x \leq 0.63$) samples (the physical origin of the antiferromagnetic alignment will be discussed later). Using the same reasoning, the smaller average exchange field energy of the Fe^{3+} tetrahedral cations compared with the Fe^{3+} octahedral cations can be explained by the likely presence of anti-phase boundaries in our films. Anti-phase boundaries increase the probability of Fe^{3+} tetrahedral cations being next-nearest neighbors, which causes these Fe^{3+} tetrahedral cations to be antiferromagnetically coupled *via* superexchange interactions,[49] resulting in a smaller average exchange field compared with the average exchange field of the Fe^{3+} octahedral cations.

Quantitative information can be obtained from the XMCD data by using well defined sum rules that relate the integration of the XAS and XMCD spectra with the orbital[60] and spin[61] magnetic moments by the equations:[62]

$$m_{orb} = -\frac{4\int_{L_3+L_2}(\mu_+ - \mu_-)d\omega}{3\int_{L_3+L_2}(\mu_+ + \mu_-)d\omega}(10 - n_{3d}) \qquad (2)$$

$$m_{spin} = -\frac{6\int_{L_3}(\mu_+ - \mu_-)d\omega - 4\int_{L_3+L_2}(\mu_+ - \mu_-)d\omega}{\int_{L_3+L_2}(\mu_+ + \mu_-)d\omega}(10 - n_{3d})\left(1 + \frac{7\langle T_z\rangle}{2\langle S_z\rangle}\right)^{-1} \quad (3)$$

where m_{orb} and m_{spin} are given in μ_B/cation and n_{3d} is the 3*d* electron occupation number per specific cation. The n_{3d} values were estimated to be 5.3 and 6.1 for Fe^{3+} and Fe^{2+} cations, respectively, from Fe 2*p* core-level photoemission[63] and 7.21 for Co^{2+}, which is expected for CoO.[59] $\langle T_z \rangle$ is the expectation value of the magnetic dipole operator and is only non-zero for systems of less than cubic symmetry.[64] In single-crystal Fe_3O_4 samples, $\langle T_z \rangle$ has been found to be negligible,[65] and since the in-plane and out-of-plane saturation magnetizations of all the samples only differ slightly, we have neglected $\langle T_z \rangle$ in our calculations.

The magnetic moments per formula unit calculated with the XMCD sum rules are compared to the magnetic moments measured with SQUID magnetometry in Fig.8(a), along with the cobalt and iron contributions to the magnetic moment. For the $Co_{1-x}Fe_{2+x}O_4$ ($0.39 \leq x \leq 1$) samples the agreement between XMCD and SQUID is very good, differing by no more than 12%; however, the agreement gets progressively worse as *x* decreases. The reason for the poor agreement for the $x = 0.01$ and 0.18 samples may be due to an overestimation of the Co^{2+} magnetic moments. Figure 8(b) shows the average orbital and spin magnetic moments per cobalt and iron cation. First considering the orbital moments, the cobalt cations have large orbital moments that increase with increasing *x* from 0.42 to 0.74 μ_B/cation. The largeness of the orbital moment is easily understood by examining the electron orbital occupations (the increase of the orbital moment with increased Fe doping will be discussed later). A $3d^7$ cation in an octahedral crystal field has two electrons to fill the three spin-down t_{2g} orbitals, while all the spin-up orbitals are already filled. Due to the tensile strain, a small tetragonal field is added, resulting in a filled d_{xy} orbital and either the d_{xz} or d_{yz} orbital being half filled, giving rise to an expected orbital

magnetic moment of 1 μ_B. Likewise, a $3d^7$ cation in a tetrahedral crystal field will have no orbital moment since the two *e* orbitals will be full. The iron orbital moments are much smaller, increasing roughly linearly with x from 0.03 to 0.12 μ_B.

The spin moments for the cobalt and iron cations behave similarly in that they increase slightly with x for the $Co_{1-x}Fe_{2+x}O_4$ ($0.01 \leq x \leq 0.39$) samples before increasing rapidly for the $Co_{0.37}Fe_{2.63}O_4$ and Fe_3O_4 samples; however, their magnitudes differ markedly, with the iron spin moments being near zero for $x \leq 0.39$. For $CoFe_2O_4$, all the iron cations are Fe^{3+} and, in a perfectly inverse spinel crystal, they do not contribute to the total magnetic moment due to the antiferromagnetic alignment of the octahedral and tetrahedral cations. This is consistent with our sum rule calculations and reveals that the majority of the magnetic moment for the $Co_{1-x}Fe_{2+x}O_4$ ($0.01 \leq x \leq 0.39$) samples is owing to the Co^{2+} cations.

IV. DISCUSSION

By using the information gained from SQUID magnetometry, XMLD and XMCD measurements, we obtain a complete picture of the magnetic structure of $Co_{1-x}Fe_{2+x}O_4$ and the cause behind the reduced magnetization of $CoFe_2O_4$ grown on higher symmetry substrates. All samples with $x < 1$ have an out-of-plane easy magnetization axis, which is caused by the large orbital moments on the Co^{2+} octahedral cations, as measured by XMCD. These orbital moments point in the out-of-plane direction owing to the small in-plane tensile strain of the samples; hence, the spins of the Co^{2+} octahedral cations will also be aligned out-of-plane because of spin-orbit coupling. However, if these spins were aligned completely in the out-of-plane direction, m_{orb} should be determined by the percentage of Co^{2+} cations that are in octahedral sites. Previous modeling of isotropic XAS spectra of the same samples determined the percentage of Co^{2+}

octahedral and tetrahedral cations to be ~ 88% and ~ 12%, respectively, for all samples with $x < 1$;[24] this would result in $m_{orb} \sim 0.88\ \mu_B$. This is much higher than the measured Co^{2+} orbital moments for the $Co_{1-x}Fe_{2+x}O_4$ ($0.01 \leq x \leq 0.39$) samples and slightly higher than the Co^{2+} orbital moment for the $Co_{0.37}Fe_{2.63}O_4$ sample, implying that the Co^{2+} cations have orbital moments that point away from and/or oppose the [001] direction. It has been shown in $CoFe_2O_4$/MgO (001) thin films that there is competition between an in-plane shape anisotropy and an out-of-plane strain-induced anisotropy.[47] Dislocations, caused by the in-plane tensile strain of the film, can induce local strains, which, because of this energy competition, may result in some of the orbital moments favoring other crystal directions. This, as a consequence, may cause a canting of the spin moments due to spin-orbit coupling. The XMLD spectra support a spin-canting model, since they show an increased spin alignment along the [001] crystal direction for the $Co_{0.37}Fe_{2.63}O_4$ compared with the $Co_{1-x}Fe_{2+x}O_4$ ($0.01 \leq x \leq 0.39$) samples, mimicking the behavior of the orbital moments. This increased spin alignment is also seen in the Fe XMLD spectra for the Fe^{2+} cations, suggesting a ferromagnetic coupling between the Fe^{2+} and Co^{2+} cations, resulting in spin canting of the Fe^{2+} cations as well.

In addition, there are two factors that support a model in which the cobalt and iron cations are also aligned antiferromagnetically within the octahedral and tetrahedral sublattices. The mixed spinel nature of $Co_{1-x}Fe_{2+x}O_4$ results in the Fe^{3+} octahedral/tetrahedral site occupancy ratio being greater than 1. The larger this ratio, the larger the probability that two Fe^{3+} cations will be next-nearest neighbors in the octahedral sublattice and have a Co^{2+} cation as their next-nearest neighbor in the tetrahedral sublattice. In this scenario, the Fe^{3+} octahedral cations will be antiferromagnetically aligned *via* superexchange since there is no Fe^{3+} tetrahedral cation to keep them both aligned ferromagnetically. This antiferromagnetic alignment will result in a reduced

magnetic moment that will change non-linearly as the Fe^{3+} octahedral/tetrahedral ratio decreases non-linearly with increasing x.[24]

The reduced magnetic moment is also attributed to the likelihood of anti-phase boundaries existing in our samples, as evidenced by the smaller average exchange field energy of Fe^{3+} tetrahedral cations compared with the Fe^{3+} octahedral cations. As mentioned above, anti-phase boundaries result in Fe^{3+} tetrahedral cations being coupled antiferromagnetically across the boundary. When the Fe^{2+}/Co^{2+} ratio is large, the double exchange interaction between the Fe^{2+} and Fe^{3+} octahedral cations is strong enough to keep the majority of the octahedral cations at the anti-phase boundary ferromagnetically aligned and not affected by the antiferromagnetic alignment of the Fe^{3+} tetrahedral cations. Because the double exchange interaction between Co^{2+} and Fe^{3+} cations is weaker than the Fe^{2+}/Fe^{3+} double exchange interaction, an increase in the number of Co^{2+} cations results in a larger percentage of octahedral cations at the anti-phase boundary being anti-ferromagnetically aligned as well. The combination of anti-phase boundaries and a partially inverse crystal structure results in it being more common for the Fe^{3+} octahedral cations to be antiferromagnetically aligned for $Co_{1-x}Fe_{2+x}O_4$ samples with small x values, even though, due to strong coupling between the Fe^{3+} octahedral and tetrahedral cations, the spin axes do not change. Since octahedral Co^{2+} and Fe^{2+} cations are coupled ferromagnetically to the Fe^{3+} octahedral cations *via* double exchange, the increased antiferromagnetic alignment of Fe^{3+} octahedral cations will result in an increased antiferromagnetic alignment of the Co^{2+} and Fe^{2+} cations as well. This is in agreement with both the XMLD spectra and the exchange field energies used in modeling the XMCD spectra. All of these factors result in a reduced magnetic moment for $CoFe_2O_4$, which tends closer to bulk values as x increases from 0 to 1 and becomes more non-linear closer to $x = 1$.

V. CONCLUSIONS

In summary, we have determined the magnetic structure of $Co_{1-x}Fe_{2+x}O_4$ by examining the bulk magnetic properties with SQUID magnetometry and the cation specific magnetic properties with XMLD and XMCD. For all samples, anti-ferromagnetic alignment of Fe^{3+} tetrahedral cations is likely caused by anti-phase boundaries, while canting among the octahedral Co^{2+} and Fe^{2+} cations is caused by strain. $Co_{1-x}Fe_{2+x}O_4$ samples with small values of x also have a large number of anti-ferromagnetically aligned Fe^{3+} octahedral cations due to a partially inverse crystal structure, the likelihood of anti-phase boundaries, and a weaker double exchange interaction between Co^{2+} and Fe^{3+} cations as compared with the Fe^{2+}/Fe^{3+} double exchange interaction. $Co_{1-x}Fe_{2+x}O_4$ samples with large x grown on higher symmetry substrates present a material in which small changes in stoichiometry can result in large changes in the magnetic moment, a result that can be utilized to tune the magnetic properties of $Co_{1-x}Fe_{2+x}O_4$ in a spintronic device.

ACKNOWLEDGEMENTS

The authors acknowledge financial support by the NSF through Grant No. MRSEC DMR 0520495 (CRISP). One of us (EN) acknowledges the support of the Army Research Office under grant #W911NF-08-1-0325 and DOE under grant DE-08NT0004115. Use of the National Synchrotron Light Source, Brookhaven National Laboratory, was supported by the U.S. Department of Energy, Office of Science, Office of Basic Energy Sciences, under Contract No. DE-AC02-98CH10886.

REFERENCES

* Present Address: Paul Scherrer Institut, 5232 Villigen PSI, Switzerland

[1] S. A. Wolf, D. D. Awschalom, R. A. Buhrman, J. M. Daughton, S. von Molnar, M. L. Roukes, A. Y. Chtchelkanova, and D. M. Treger, Science **294**, 1488 (2001).

[2] I. Zutic, J. Fabian, and S. Das Sarma, Rev. Mod. Phys. **76**, 323 (2004).

[3] J. Cibert, J. F. Bobo, and U. Luders, C. R. Phys. **6**, 977 (2005).

[4] C. H. Ahn, A. Bhattacharya, M. Di Ventra, J. N. Eckstein, C. D. Frisbie, M. E. Gershenson, A. M. Goldman, I. H. Inoue, J. Mannhart, A. J. Millis, A. F. Morpurgo, D. Natelson, and J. M. Triscone, Rev. Mod. Phys. **78**, 1185 (2006).

[5] J. H. Haeni, P. Irvin, W. Chang, R. Uecker, P. Reiche, Y. L. Li, S. Choudhury, W. Tian, M. E. Hawley, B. Craigo, A. K. Tagantsev, X. Q. Pan, S. K. Streiffer, L. Q. Chen, S. W. Kirchoefer, J. Levy, and D. G. Schlom, Nature (London) **430**, 758 (2004).

[6] A. Moreo, S. Yunoki, and E. Dagotto, Science **283**, 2034 (1999).

[7] A. Urushibara, Y. Moritomo, T. Arima, A. Asamitsu, G. Kido, and Y. Tokura, Phys. Rev. B **51**, 14103 (1995).

[8] J. O'Donnell, A. E. Andrus, S. Oh, E. V. Colla, and J. N. Eckstein, Appl. Phys. Lett. **76**, 1914 (2000).

[9] G. Hu and Y. Suzuki, Phys. Rev. Lett. **89**, 276601 (2002).

[10] A. V. Ramos, M. J. Guittet, J. B. Moussy, R. Mattana, C. Deranlot, F. Petroff, and C. Gatel, Appl. Phys. Lett. **91**, 122107 (2007).

[11] U. Luders, M. Bibes, K. Bouzehouane, E. Jacquet, J. P. Contour, S. Fusil, J. F. Bobo, J. Fontcuberta, A. Barthelemy, and A. Fert, Appl. Phys. Lett. **88**, 082505 (2006).

[12] H. Zheng, J. Wang, S. E. Lofland, Z. Ma, L. Mohaddes-Ardabili, T. Zhao, L. Salamanca-Riba, S. R. Shinde, S. B. Ogale, F. Bai, D. Viehland, Y. Jia, D. G. Schlom, M. Wuttig, A. Roytburd, and R. Ramesh, Science **303**, 661 (2004).

[13] W. Eerenstein, M. Wiora, J. L. Prieto, J. F. Scott, and N. D. Mathur, Nature Mater. **6**, 348 (2007).

[14] H. J. A. Molegraaf, J. Hoffman, C. A. F. Vaz, S. Gariglio, D. van der Marel, C. H. Ahn, and J. M. Triscone, Adv. Mater. **21**, 3470 (2009).

[15] C. A. F. Vaz, J. Hoffman, Y. Segal, J. W. Reiner, R. D. Grober, Z. Zhang, C. H. Ahn, and F. J. Walker, Phys. Rev. Lett. **104**, 127202 (2010).

[16] P. I. Slick, in *Ferromagnetic Materials: A Handbook on the Properties of Magnetically Ordered Substances*, edited by E. P. Wohlfarth (North-Holland Publishing Company, Amsterdam, 1980), Vol. 2, p. 189.

[17] Z. Szotek, W. M. Temmerman, D. Kodderitzsch, A. Svane, L. Petit, and H. Winter, Phys. Rev. B **74**, 174431 (2006).

[18] V. N. Antonov, B. N. Harmon, and A. N. Yaresko, Phys. Rev. B **67**, 024417 (2003).

[19] H.-T. Jeng and G. Y. Guo, J. Magn. Magn. Mater. **239**, 88 (2002).

[20] Z. Zhang and S. Satpathy, Phys. Rev. B **44**, 13319 (1991).

[21] M. Penicaud, B. Siberchicot, C. B. Sommers, and J. Kubler, J. Magn. Magn. Mater. **103**, 212 (1992).

[22] C. D. Owens, Proc. IRE **44**, 1234 (1956).

[23] J. Takaobushi, M. Ishikawa, S. Ueda, E. Ikenaga, J.-J. Kim, M. Kobata, Y. Takeda, Y. Saitoh, M. Yabashi, Y. Nishino, D. Miwa, K. Tamasaku, T. Ishikawa, I. Satoh, H. Tanaka, K. Kobayashi, and T. Kawai, Phys. Rev. B **76**, 205108 (2007).

[24] J. A. Moyer, C. A. F. Vaz, E. Negusse, D. A. Arena, and V. E. Henrich, Phys. Rev. B **83**, 035121 (2011).

[25] D. Tripathy, A. O. Adeyeye, C. B. Boothroyd, and S. N. Piramanayagam, J. Appl. Phys. **101**, 013904 (2007).

[26] J. Takaobushi, H. Tanaka, T. Kawai, S. Ueda, J.-J. Kim, M. Kobata, E. Ikenaga, M. Yabashi, K. Kobayashi, Y. Nishino, D. Miwa, K. Tamasaku, and T. Ishikawa, Appl. Phys. Lett. **89**, 242507 (2006).

[27] S. Ueda, H. Tanaka, J. Takaobushi, E. Ikenaga, J.-J. Kim, M. Kobata, T. Kawai, H. Osawa, N. Kawamura, M. Suzuki, and K. Kobayashi, Appl. Phys. Express **1**, 077003 (2008).

[28] D. Venkateshvaran, M. Althammer, A. Nielsen, S. Geprags, M. S. RamachandraRao, S. T. B. Goennenwein, M. Opel, and R. Gross, Phys. Rev. B **79**, 134405 (2009).

[29] J. Stohr and H. C. Siegmann, *Magnetism: From Fundamentals to Nanoscale Dynamics* (Springer, Berlin, 2006).

[30] D. J. Huang, C. F. Chang, H.-T. Jeng, G. Y. Guo, H.-J. Lin, W. B. Wu, H. C. Ku, A. Fujimori, Y. Takahashi, and C. T. Chen, Phys. Rev. Lett. **93**, 077204 (2004).

[31] G. Hu, J. H. Choi, C. B. Eom, V. G. Harris, and Y. Suzuki, Phys. Rev. B **62**, R779 (2000).

[32] G. A. Sawatzky, F. van der Woude, and A. H. Morrish, Phys. Rev. **187**, 747 (1969).

[33] S. A. Chambers, R. F. C. Farrow, S. Maat, M. F. Toney, L. Folks, J. G. Catalano, T. P. Trainor, and G. E. Brown Jr., J. Magn. Magn. Mater. **246**, 124 (2002).

[34] Y. Suzuki, G. Hu, R. B. van Dover, and R. J. Cava, J. Magn. Magn. Mater. **191**, 1 (1999).

[35] F. Rigato, J. Geshev, V. Skumryev, and J. Fontcuberta, J. Appl. Phys. **106**, 113924 (2009).

[36] G. Hu, V. G. Harris, and Y. Suzuki, IEEE Trans. Magn. **37**, 2347 (2001).

[37] M. Tachiki, Prog. Theor. Phys. **23**, 1055 (1960).

[38] J. C. Slonczewski, Phys. Rev. **110**, 1341 (1958).

[39] J. C. Slonczewski, J. Appl. Phys. **29**, 448 (1958).

[40] G. F. Dionne, *Magnetic Oxides* (Springer Science+Business Media, LLC, Boston, 2009).

[41] L. Horng, G. Chern, M. C. Chen, P. C. Kang, and D. S. Lee, J. Magn. Magn. Mater. **270**, 389 (2004).

[42] R. V. Chopdekar and Y. Suzuki, Appl. Phys. Lett. **89**, 182506 (2006).

[43] F. Zavaliche, H. Zheng, L. Mohaddes-Ardabili, S. Y. Yang, Q. Zhan, P. Shafer, E. Reilly, R. Chopdekar, Y. Jia, P. Wright, D. G. Schlom, Y. Suzuki, and R. Ramesh, Nano Letters **5**, 1793 (2005).

[44] Y. Zhang, C. Y. Deng, J. Ma, Y. H. Lin, and C. W. Nan, Appl. Phys. Lett. **92**, 062911 (2008).

[45] J. H. Park, J. H. Lee, M. G. Kim, Y. K. Jeong, M. A. Oak, H. M. Jang, H. J. Choi, and J. F. Scott, Phys. Rev. B **81**, 6 (2010).

[46] G. Bate, in *Ferromagnetic Materials: A Handbook on the Properties of Magnetically Ordered Substances*, edited by E. P. Wohlfarth (North-Holland Publishing Company, Amsterdam, 1980), Vol. 2, p. 381.

[47] A. Lisfi, C. M. Williams, L. T. Nguyen, J. C. Lodder, A. Coleman, H. Corcoran, A. Johnson, P. Chang, A. Kumar, and W. Morgan, Phys. Rev. B **76**, 054405 (2007).

[48] D. T. Margulies, F. T. Parker, and A. E. Berkowitz, J. Appl. Phys. **75**, 6097 (1994).

[49] D. T. Margulies, F. T. Parker, M. L. Rudee, F. E. Spada, J. N. Chapman, P. R. Aitchison, and A. E. Berkowitz, Phys. Rev. Lett. **79**, 5162 (1997).

[50] B. T. Thole, G. Vanderlaan, and G. A. Sawatzky, Phys. Rev. Lett. **55**, 2086 (1985).

[51] F. M. F. de Groot, J. C. Fuggle, B. T. Thole, and G. A. Sawatzky, Phys. Rev. B **42**, 5459 (1990).

[52] G. van der Laan and I. W. Kirkman, J. Phys.: Condens. Matter **4**, 4189 (1992).

[53] G. van der Laan and B. T. Thole, Phys. Rev. B **43**, 13401 (1991).

[54] E. Stavitski and F. M. F. de Groot, Micron **41**, 687 (2010).

[55] R. D. Cowan, *The Theory of Atomic Structure and Spectra* (University of California Press, Berkeley, 1981).

[56] P. Kuiper, B. G. Searle, P. Rudolf, L. H. Tjeng, and C. T. Chen, Phys. Rev. Lett. **70**, 1549 (1993).

[57] P. Kuiper, B. G. Searle, L.-C. Duda, R. M. Wolf, and P. J. van der Zaag, J. Electron Spectrosc. Relat. Phenom. **86**, 107 (1997).

[58] E. Arenholz, G. van der Laan, R. V. Chopdekar, and Y. Suzuki, Phys. Rev. B **74**, 094407 (2006).

[59] G. van der Laan, E. Arenholz, R. V. Chopdekar, and Y. Suzuki, Phys. Rev. B **77**, 064407 (2008).

[60] B. T. Thole, P. Carra, F. Sette, and G. Vanderlaan, Phys. Rev. Lett. **68**, 1943 (1992).

[61] P. Carra, B. T. Thole, M. Altarelli, and X. D. Wang, Phys. Rev. Lett. **70**, 694 (1993).

[62] C. T. Chen, Y. U. Idzerda, H. J. Lin, N. V. Smith, G. Meigs, E. Chaban, G. H. Ho, E. Pellegrin, and F. Sette, Phys. Rev. Lett. **75**, 152 (1995).

[63] T. Saitoh, A. E. Bocquet, T. Mizokawa, and A. Fujimori, Phys. Rev. B **52**, 7934 (1995).

[64] J. Stohr and H. Konig, Phys. Rev. Lett. **75**, 3748 (1995).

[65] E. Goering, S. Gold, M. Lafkioti, and G. Schutz, Europhys. Lett. **73**, 97 (2006).

TABLE AND FIGURE CAPTIONS

TABLE I. Average magnetic exchange field energies, $g\mu H$, used in calculating the LFM XMCD spectra given in units of meV.

FIG. 1. (Color online) (a) Schematic of the spinel crystal structure, which is based on an oxygen FCC sublattice with the cations occupying interstitial sites: 1/3 of the cations are located in 1/8 of the available tetrahedral sites, and 2/3 of the cations are located in 1/2 of the available octahedral sites. (b) Illustration of the magnetic interactions in Fe_3O_4. The Fe^{3+} octahedral and tetrahedral cations are coupled antiferromagnetically *via* the superexchange (SE) interaction, and the Fe^{3+} and Fe^{2+} octahedral cations are coupled ferromagnetically *via* the double exchange (DE) interaction. Arrows located on cations represent sizes of magnetic moments. (c) Illustration of the magnetic interactions in $CoFe_2O_4$. Magnetic interactions are the same as Fe_3O_4, with Fe^{2+} cation replaced by Co^{2+}.

FIG. 2. (Color online) In-plane *M-H* loops of $Co_{1-x}Fe_{2+x}O_4$ samples with $0.01 \leq x \leq 1$ at (a) 100 K and (b) 300 K with the magnetic field aligned along the [010] direction, and out-of-plane *M-H* loops at (c) 100 K and (d) 300 K with the magnetic field aligned along the [001] direction.

FIG. 3. (Color online) Comparison of in-plane and out-of-plane coercive fields at (a) 100 K and (b) 300K, and in-plane and out-of-plane saturation and remnant magnetizations at (c) 100 K and (d) 300 K vs stoichiometry.

FIG. 4. (Color online) (a) Interpolated Co 2*p* XAS spectra for $Co_{0.37}Fe_{2.63}O_4$ with electric field perpendicular and parallel to the [001] crystal direction, and the corresponding XMLD spectrum. (b) Co 2*p* XMLD spectra for $Co_{1-x}Fe_{2+x}O_4$ samples with $x = 0.01, 0.18, 0.39, 0.63$. (c) Comparison between the measured Co 2*p* XMLD spectrum, the calculated LFM spectrum, and the individual LFM spectra for the Co^{2+} octahedral and tetrahedral cations.

FIG. 5. (Color online) (a) Interpolated Fe 2*p* XAS spectra for $Co_{0.37}Fe_{2.63}O_4$ with electric field perpendicular and parallel to the [001] crystal direction, and the corresponding XMLD spectrum. (b) Fe 2*p* XMLD spectra for $Co_{1-x}Fe_{2+x}O_4$ samples with $x = 0.01, 0.18, 0.39, 0.63, 1$. (c) Comparison between the measured Fe 2*p* XMLD spectrum, the calculated LFM spectrum, and the individual LFM spectra for the Fe^{2+} octahedral, Fe^{3+} octahedral, and Fe^{3+} tetrahedral cations.

FIG. 6. (Color online) (a) Experimental Co 2*p* XAS spectra for $Co_{0.99}Fe_{2.01}O_4$ with a positive (μ^+) and negative (μ^+) magnetic field, and the corresponding XMCD spectrum. (b) Experimental Co 2*p* XMCD spectra for $Co_{1-x}Fe_{2+x}O_4$ samples with $x = 0.01, 0.18, 0.39, 0.63$. (c) Comparison between the experimental Co 2*p* XMCD spectrum, the calculated LFM spectrum, and the individual LFM spectra for the Co^{2+} octahedral and tetrahedral cations.

FIG. 7. (Color online) (a) Experimental Fe 2*p* XAS spectra for Fe_3O_4 with a positive (μ^+) and negative (μ^+) magnetic field, and the corresponding XMCD spectrum. (b) Experimental Fe 2*p* XMCD spectra for $Co_{1-x}Fe_{2+x}O_4$ samples with $x = 0.01, 0.18, 0.39, 0.63, 1$. (c) Comparison between the experimental Fe 2*p* XMCD spectrum, the calculated LFM spectrum, and the individual LFM spectra for the Fe^{2+} octahedral, Fe^{3+} octahedral, and Fe^{3+} tetrahedral cations.

FIG. 8. (Color online) (a) Comparison of out-of-plane magnetic moments per f.u. as determined by SQUID and XMCD sum rules vs stoichiometry. Also included are the cobalt and iron contributions to the magnetic moment as determined by XMCD. (b) Comparison of the average orbital and spin magnetic moments per cobalt and iron cation vs stoichiometry as determined by XMCD sum rules.

Sample	Co^{2+} oct and tet	Fe^{2+} oct	Fe^{3+} oct	Fe^{3+} tet
$Co_{0.99}Fe_{2.01}O_4$	6.2	6.4	6.7	5.9
$Co_{0.82}Fe_{2.18}O_4$	6.7	6.2	6.5	5.9
$Co_{0.61}Fe_{2.39}O_4$	7.1	5.1	6.3	5.2
$Co_{0.37}Fe_{2.63}O_4$	12.9	8.3	11.3	8.2
Fe_3O_4		27.4	27.4	19.4

TABLE I, J. A. Moyer, Physical Review B

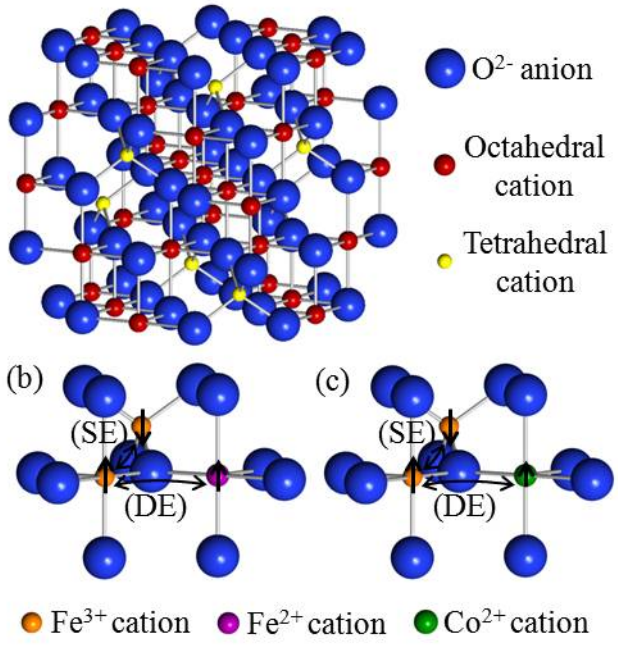

FIG. 1, J. A. Moyer, Physical Review B

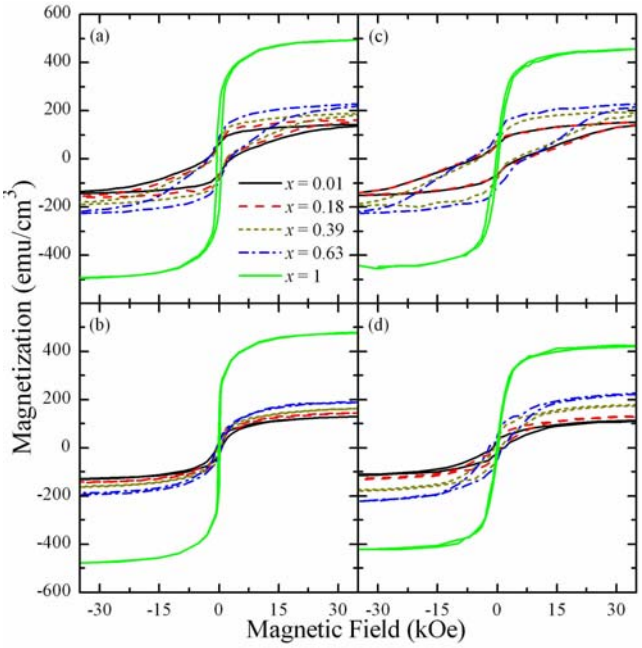

FIG. 2, J. A. Moyer, Physical Review B

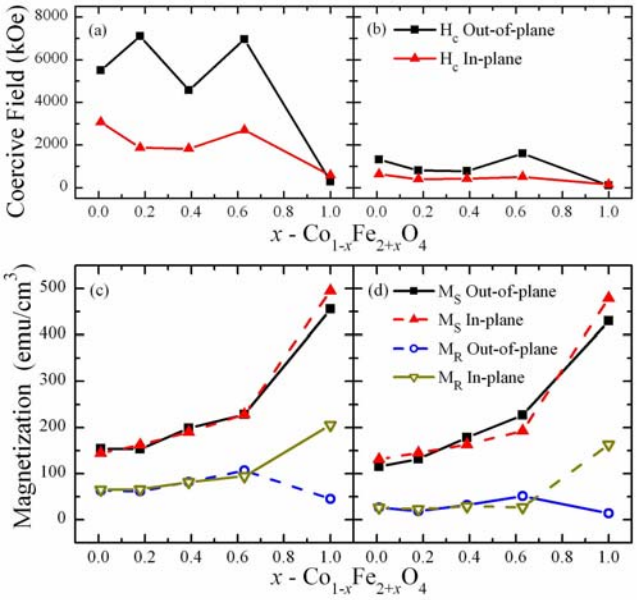

FIG. 3, J. A. Moyer, Physical Review B

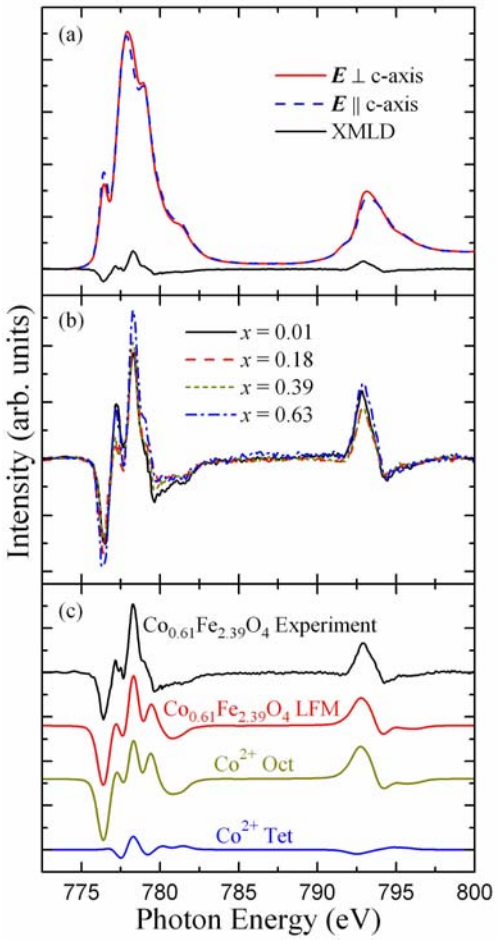

FIG. 4, J. A. Moyer, Physical Review B

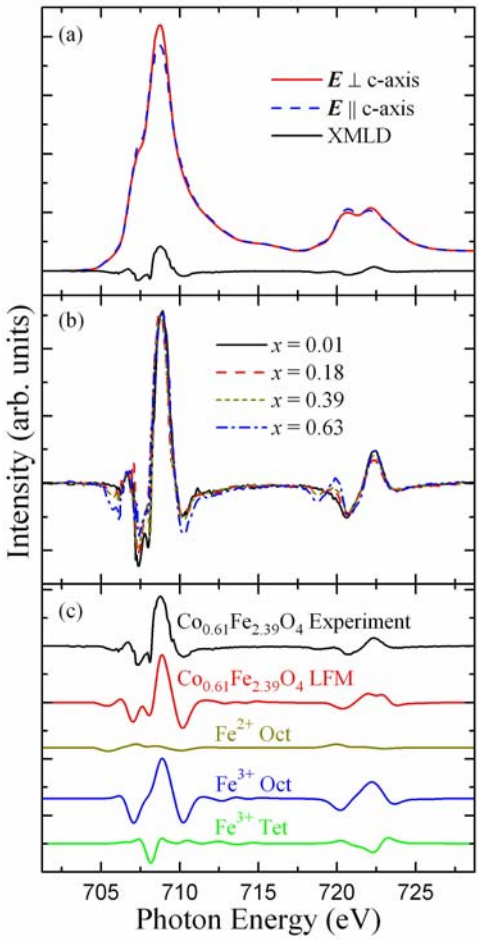

FIG. 5, J. A. Moyer, Physical Review B

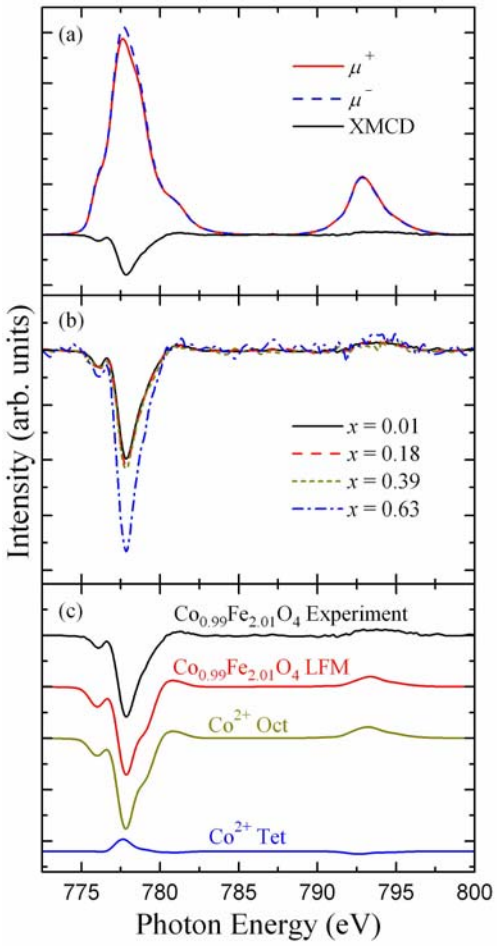

FIG. 6, J. A. Moyer, Physical Review B

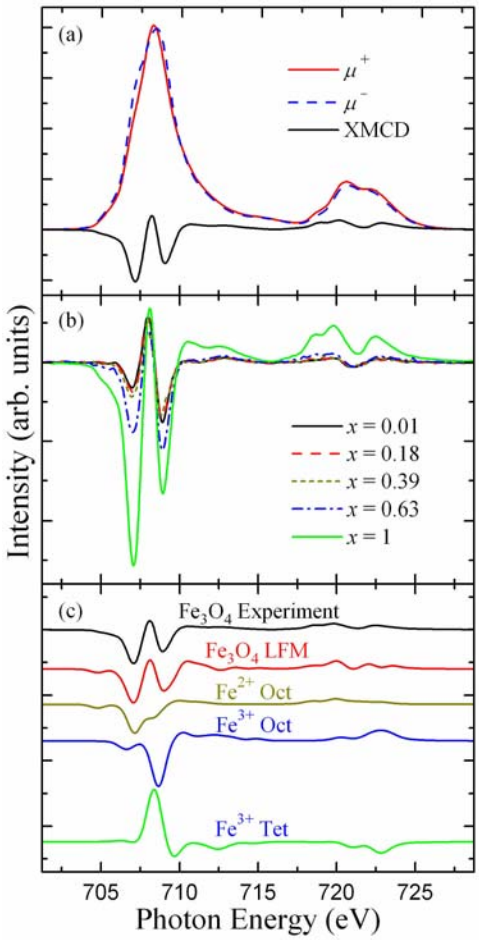

FIG. 7, J. A. Moyer, Physical Review B

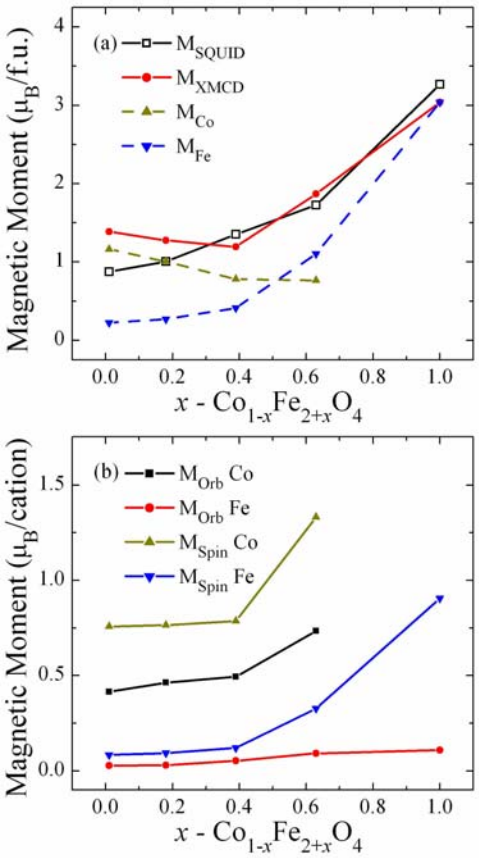

FIG. 8, J. A. Moyer, Physical Review B